






Article

Wind Turbine Active Fault Tolerant Control Based on Backstepping Active Disturbance Rejection Control and a Neurofuzzy Detector

Hamza Assia ^{1,*}, Houari Merabet Boulouiha ¹, William David Chicaiza ², Juan Manuel Escaño ², Abderrahmane Kacimi ³, José Luis Martínez-Ramos ^{4,*} and Mouloud Denai ⁵

- ¹ Department of Electrical Engineering, Laboratory of Automation and Systems Analysis (LAAS), National Polytechnic School of Oran (Maurice Audin), Oran 31000, Algeria; houari.merabet-boulouiha@enp-oran.dz
- ² Department of System Engineering and Automatic Control, University of Seville, 41092 Seville, Spain; wchicaiza@us.es (W.D.C.); jescano@us.es (J.M.E.)
- ³ Department of Instrumentation Maintenance, Institute of Maintenance and Industrial Safety, Oran 31000, Algeria; kacimi.abderrahmane@univ-oran2.dz
- ⁴ Department of Electrical Engineering, University of Seville, 41092 Seville, Spain
- ⁵ Department of Engineering and Technology, University of Hertfordshire, Hatfield AL10 9AB, UK; m.denai@herts.ac.uk
- * Correspondence: hamza.assia@enp-oran.dz (H.A.); camel@us.es (J.L.M.-R.)

Abstract: Wind energy conversion systems have become an important part of renewable energy history due to their accessibility and cost-effectiveness. Offshore wind farms are seen as the future of wind energy, but they can be very expensive to maintain if faults occur. To achieve a reliable and consistent performance, modern wind turbines require advanced fault detection and diagnosis methods. The current research introduces a proposed active fault-tolerant control (AFTC) system that uses backstepping active disturbance rejection theory (BADRC) and an adaptive neurofuzzy system (ANFIS) detector in combination with principal component analysis (PCA) to compensate for system disturbances and maintain performance even when a generator actuator fault occurs. The simulation outcomes demonstrate that the suggested method successfully addresses the actuator generator torque failure problem by isolating the faulty actuator, providing a reliable and robust solution to prevent further damage. The neurofuzzy detector demonstrates outstanding performance in detecting false data in torque, achieving a precision of 90.20% for real data and 100% for false data. With a recall of 100%, no false negatives were observed. The overall accuracy of 95.10% highlights the detector's ability to reliably classify data as true or false. These findings underscore the robustness of the detector in detecting false data, ensuring the accuracy and reliability of the application presented. Overall, the study concludes that BADRC and ANFIS detection and isolation can improve the reliability of offshore wind farms and address the issue of actuator generator torque failure.

Keywords: active fault-tolerant control; backstepping; active disturbance rejection control; adaptive neurofuzzy inference system; principal component analysis



Citation: Assia, H.; Merabet Boulouiha, H.; Chicaiza, W.D.; Escaño, J.M.; Kacimi, A.; Martínez-Ramos, J.L.; Denai, M. Wind Turbine Active Fault Tolerant Control Based on Backstepping Active Disturbance Rejection Control and a Neurofuzzy Detector. *Energies* **2023**, *16*, 5455. <https://doi.org/10.3390/en16145455>

Academic Editor: Frede Blaabjerg

Received: 31 May 2023

Revised: 1 July 2023

Accepted: 10 July 2023

Published: 18 July 2023



Copyright: © 2023 by the authors. Licensee MDPI, Basel, Switzerland. This article is an open access article distributed under the terms and conditions of the Creative Commons Attribution (CC BY) license (<https://creativecommons.org/licenses/by/4.0/>).

1. Introduction

The global community's focus on environmental issues and clean energy has intensified significantly, resulting in substantial progress and notable achievements. These efforts align harmoniously with global initiatives such as the Sustainable Development Goals (SDGs) and the pursuit of net zero targets, reaffirming the unwavering commitment to global sustainability objectives. One prominent renewable energy source is wind. Harvested for thousands of years already, wind-driven electric generation systems are securing the use of that form of energy for many years in the future. It is clean, secure, and abundant. This implies that making wind turbines as fault tolerant as possible is a profitable long-term endeavour. However, wind power is sporadic and unpredictable. It

is also challenging to use wind turbines to their full potential because of their nonlinear properties. The power fluctuations produced by wind turbines are caused by random fluctuations in wind speed [1], although it was proven in [2] that slotted airfoil profiles are effective in improving the efficiency of wind turbines. The term MPPT (Maximum Power Point Tracking) control refers to a variety of research techniques used to monitor the wind turbine's peak output [3]. On the other hand, one of the key problems with wind power generation systems is wind turbine failure [4]. These failures are a result of faults that develop in the wind turbine and may be directly attributable to sensors, actuators, or the system itself [5]. Applying novel fault-tolerant control (FTC) methods to contemporary wind turbines has the potential to improve efficiency [6].

In recent years, numerous writers have put forward schemes for fault detection and isolation (FDI) that rely on the measurements derived from data sensors. This development has sparked significant interest in data-driven approaches, where the primary focus lies on feature extraction and classification techniques. Two methods were employed in study [7] to isolate faults at different locations. Support Vector Machines (SVMs) utilise data and feature vectors to effectively identify and isolate most faults, and use a Kalman filter observer for high varying dynamics. Another study [8] proposed an FDI method that employs an FDI benchmark model for wind turbines that combines multiple SVMs with kernels of radius basis functions to detect and identify sensor stuck faults and offset. In [9], deep neural networks (DNN) and principal component analysis (PCA) are utilised to address the challenges posed by big data, inaccurate fault diagnosis, and incorrect fault detection in wind farms. The PCA algorithm is used to reduce data dimensions, focusing primarily on minimising redundancy and improving the accuracy of fault diagnosis. In [10], a model-based fault diagnosis and isolation methodology was developed for wind turbines using a set of analytical redundancy relations (ARRs) acquired from a fault signature matrix that considers the correlation between ARRs and faults and the structural analysis of the wind turbine model. In [11], a DNN was used to adjust the parameters of linear active disturbance rejection control to regulate the control parameters of the wind turbine according to the measured states. In [12], a sensor fault detection and isolation strategy is developed using convex state observers to generate residuals. The fault diagnosis method employs an ANFIS method to derive a collection of polytopic-based linear representations and membership functions to interpolate the linear models of the convex Takagi–Sugeno model. A prediction model using three artificial intelligence techniques based on the application of a new fault detection methodology combined with ADRC was used in [13], which is used to control the system and nullify the effects of disturbances generated by the fault. In [14], a hybrid methodology was developed to detect and isolate fault-based quasi-Linear Parameter Varying (qLPV) zonotopic observers and ANFIS. FDI is based on the residual generation obtained by a bank of zonotopic observers of qLPV of the identified models; also, in [15], a bank of observers of sliding mode was designed to create an FDI system for actuator faults. However, this method was not integrated into an FTC system and it is observed that the chattering was evident in the results of this method.

In the work presented in [16], the discrepancy is detected indirectly, using the residual generated between the measured and estimated power value to design an FDI and FTC for the failure of the generator actuator.

The novelty of this work lies in its ability to detect discrepancies between direct torque values and their data-driven neurofuzzy models that facilitate early and precise detection and isolation. Furthermore, the incorporation of backstepping control, a linear observer of active disturbance rejection control, and neurofuzzy techniques enhance robustness, enabling an active fault tolerance control (AFTC) approach for wind turbines. This research demonstrates how the AFTC approach can be employed effectively for fault detection and isolation in real wind turbine systems.

In order to achieve the greatest power point tracking of the wind turbine, a robust backstepping based on an active disturbance rejection controller was presented under actuator failure. First, the backstepping term was used to handle both external and internal

system disturbances due to its robustness and synthesis, which is based on a stability study of the overall system. Then, for linear ADRC, a Luenberger observer is employed for estimating the value of the generator torque to counteract the influence of the torque actuator failure that decreases the extraction of power. Lastly, for the diagnosis and isolation process, an ANFIS algorithm based on PCA was used to detect and manage the situation between the measured and the observed value of the generator torque. The subsequent parts of this manuscript outline the structure as the following. In Section 2, which follows the introduction, a wind turbine, gearbox, shaft and generator are modeled as well as the properties that are involved throughout the paper with a discussion about the MPPT. The synthesis and design of the proposed AFTC law are presented in Section 3, with a demonstration analysis of the robustness of the suggested FTC and the architecture of the FDI based on the neurofuzzy system. Section 4 summarises the results achieved with the strategy employed for fault detection and diagnosis in wind turbines. A comparative analysis has been included to establish the potential advantages of the proposed approach in relation to existing methods. Additionally, a subsection that discusses the limitations and challenges of the proposed method has been included. Finally, the main conclusions are provided in Section 5.

2. Wind Power System Modeling

2.1. Wind Turbine Model

The wind turbine aerodynamic power has a nonlinear expression that is a function relating to the radius of the rotor R , the speed of the wind V_w , the density of air ρ_{air} and the power coefficient C_p [17],

$$P_{aer} = \frac{1}{2} C_p(\lambda, \beta) \rho_{air} \pi R^2 V_w^3 \quad (1)$$

where C_p denotes the power coefficient, and C_p is related to two parameters, the blade pitch angle β and the tip-speed ratio λ [18].

$$C_p = 0.5 + 0.0167(3 - \beta) \sin(\lambda_i) + 0.00184(3 - \lambda_i) \quad (2)$$

$$\lambda_i = \frac{(0.1 + \lambda)\pi}{14.8 + 0.3(2 - \beta)} \quad (3)$$

The ratio λ is a function of the shaft's angular velocity ω_t , wind speed V_w and the rotor radius R [19].

$$\lambda = \frac{\omega_t R}{V_w} \quad (4)$$

where ω_t is the turbine speed.

The highest value of $C_{p_{max}}$ and a specified value of λ are used to describe the most favourable value of the ratio λ_{opt} , which is the optimal speed ratio, and those are the circumstances that allow the employment of MPPT control [20].

The highest speed of the turbine extracted from the wind is provided by,

$$\omega_{t_{opt}} = \frac{\lambda_{opt} V_w}{R} \quad (5)$$

2.2. Model Gearbox

The high-speed and low-speed shafts (HSS/LSS) of the generator ω_g and the turbine ω_t are coupled by the gearbox. Assuming that the multiplier is perfect, i.e., the mechanical losses are insignificant, the multiplier can be represented by a gain N_g , where N_g is a simple constant [21].

$$\omega_t = \frac{\omega_g}{N_g} \quad (6)$$

$$\tau_g = \frac{\tau_t}{N_g} \quad (7)$$

where τ_g and τ_t are torques of the generator and turbine, respectively.

2.3. Dynamic Model of Shaft

The shaft consists of the rotor's inertia-matched mass that also houses the hub, blades and the generator's rotor with a small additional inertia. Total inertia J is the aggregate of the turbine's rotational inertia J_t and the inertia of the generator J_g brought backward to the turbine's rotor [22].

$$J = \frac{J_t}{N_g^2} + J_g \quad (8)$$

In general, the shaft's mechanical equation, incorporating the masses of the generator and turbine, is given by [23],

$$J \frac{d\omega_g}{dt} + f\omega_g = \tau_g - \tau_{em} \quad (9)$$

where τ_{em} , ω_g and f are the electromagnetic torque, the mechanical speed and the generator viscous friction coefficient, respectively.

The correlation between the speed of the generator ω_g , power P_g and the torque τ_g is given by,

$$\tau_g N_g = \frac{P_g}{\omega_g} \quad (10)$$

2.4. Generator Model

The wind turbine is connected to a double fed induction generator (DFIG) through a gearbox. The given equations describe the voltage equations of the generator's stator and rotor model in the d-q axis [24],

$$\begin{cases} V_{sd} = R_s I_{sd} + \frac{d\phi_{sd}}{dt} - \omega_s \phi_{sq} \\ V_{sq} = R_s I_{sq} + \frac{d\phi_{sq}}{dt} + \omega_s \phi_{sd} \\ V_{rd} = R_r I_{rd} + \frac{d\phi_{rd}}{dt} - \omega_r \phi_{rq} \\ V_{rq} = R_r I_{rq} + \frac{d\phi_{rq}}{dt} + \omega_r \phi_{rd} \end{cases} \quad (11)$$

The equations provided represent the flux equations of the generator rotor and stator model, specifically in the d-q axis,

$$\begin{cases} \phi_{sd} = L_s I_{sd} + M I_{rd} \\ \phi_{sq} = L_s I_{sq} + M I_{rq} \\ \phi_{rd} = L_r I_{rd} + M I_{sd} \\ \phi_{rq} = L_r I_{rq} + M I_{sq} \end{cases} \quad (12)$$

2.5. Maximum Power Point Tracking

In response to how fast the wind is blowing, the turbine can work in two different modes: nominal power and maximum power point tracking (MPPT). As demonstrated in Figure 1, when the speed of the wind lies between the nominal speed and the cut-in speed, the turbine will work in MPPT mode, which requires the highest power conversion coefficient C_p . When the speed of wind falls under the predetermined cut-in speed, the wind turbine ceases its operation due to insufficient energy to initiate rotor movement. Similarly, if the speed of wind goes beyond the designated nominal threshold, the wind turbine shuts down as a precautionary measure to prevent any potential damage to the blades [25].

The key aim of the MPPT control technique is to get the most power from the wind, and the generator is operated at its highest possible speed. This is done by changing the wind turbine rotation speed when the wind speed is less than the value rated. This ideal speed is reached when the ratio λ is most effective. To reach this ideal λ , the electromagnetic torque has to be adjusted and approximated using the MPPT strategy [26].

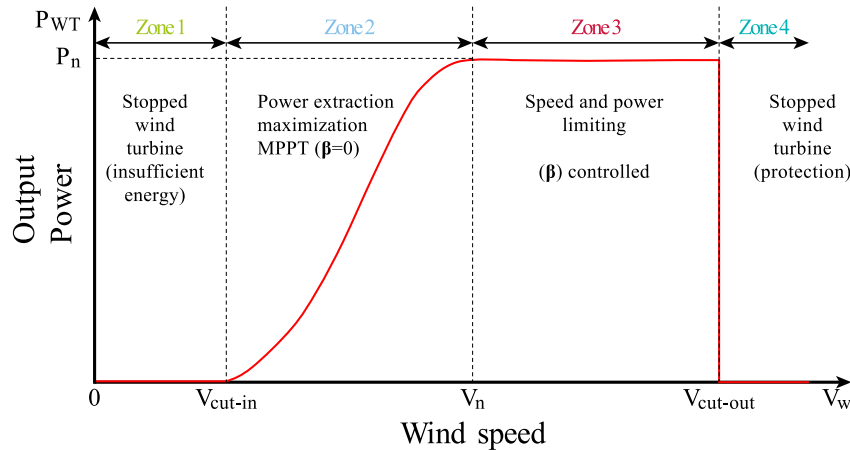


Figure 1. Characteristic of the power curve versus the speed of wind.

3. Design of the AFTC Based on the BADRC and ANFIS

3.1. Design of FTC Based on the Backstepping ADRC Technique

Our aim is to design a robust backstepping control system based on the ADRC approach, which is able to approximate an unidentified understanding of the actuator torque of the generator (event of a generator/converter fault) and avoid its impact on the controlling law, with the objective of accomplishing a precise tracking of the intended trajectory and providing an effective FTC.

Let us introduce $x_1 = \omega_{mes}$ and $x_2 = \tau_g$, the state variables, Equation (9) could be reformulated as,

$$\begin{cases} \dot{x}_1 = \frac{1}{J}(x_2 - f x_1 - u) \\ \dot{x}_2 = z \end{cases} \tag{13}$$

where the system's input is $u(t) = \tau_{em}$ and z is an unknown input. A state space representation of the affected system represented by Equation (13) is required to derive the estimator,

$$\begin{cases} \begin{pmatrix} \dot{x}_1(t) \\ \dot{x}_2(t) \end{pmatrix} = \underbrace{\begin{pmatrix} -f/J & 1/J \\ 0 & 0 \end{pmatrix}}_A \cdot \begin{pmatrix} x_1(t) \\ x_2(t) \end{pmatrix} + \underbrace{\begin{pmatrix} -1/J \\ 0 \end{pmatrix}}_B u(t) + \begin{pmatrix} 0 \\ 1 \end{pmatrix} z \\ y(t) = \underbrace{(1 \ 0)}_C \begin{pmatrix} x_1(t) \\ x_2(t) \end{pmatrix} \end{cases} \tag{14}$$

Due to the fact that the virtual input z is unable to be measured, a state observer is only capable of being built using an input from the system $u(t)$ and $y(t)$ an output from the system. On the contrary, a rough estimate of state $x_2(t)$ will offer an accurate approximation of τ_g , i.e., $\hat{\tau}_g$, if the actual value of the generalised disturbance is identical to $\tau_g(t)$, which can be thought of as a piecewise constant. The mathematical formulas that describe the extended state observer (a generalised disturbance extends the integrator process) are provided in Equation (15). It should be noted that a Luenberger observer is utilised for linear ADRC [27].

$$\begin{pmatrix} \hat{x}_1(t) \\ \hat{x}_2(t) \end{pmatrix} = \begin{pmatrix} -f/J & 1/J \\ 0 & 0 \end{pmatrix} \cdot \begin{pmatrix} \hat{x}_1(t) \\ \hat{x}_2(t) \end{pmatrix} + \begin{pmatrix} -1/J \\ 0 \end{pmatrix} \cdot u(t) + \begin{pmatrix} l_1 \\ l_2 \end{pmatrix} \cdot \underbrace{C \begin{pmatrix} e_1(t) \\ e_2(t) \end{pmatrix}}_e \tag{15}$$

with $C.e = e_1 = \omega_{mes} - \hat{\omega} = x_1 - \hat{x}_1$ and $l_1, l_2 > 0$ must be chosen for a desired error dynamic. Let the error dynamic be given by,

$$\begin{pmatrix} \dot{e}_1(t) \\ \dot{e}_2(t) \end{pmatrix} = A \cdot \begin{pmatrix} e_1(t) \\ e_2(t) \end{pmatrix} - \begin{pmatrix} l_1 \\ l_2 \end{pmatrix} \cdot Ce + \begin{pmatrix} 0 \\ 1 \end{pmatrix} z \quad (16)$$

$$\begin{pmatrix} \dot{e}_1(t) \\ \dot{e}_2(t) \end{pmatrix} = (A - LC)e + \begin{pmatrix} 0 \\ 1 \end{pmatrix} z \quad (17)$$

Combining Equations (16) and (17) with our BADRC theory, the proposed controller is presented as,

$$\tau_{em_{ref}} = -J\dot{\omega}_{ref} - f\hat{\omega} + \hat{\tau}_g - k(\omega_{ref} - \hat{\omega}) \quad (18)$$

Assuming that z is bounded $|z| < \max(\delta\tau_g)$ and the Hurwitz matrix is $A - LC$, the erroneous dynamics exhibit exponential stability [28].

To facilitate tuning simplicity, the whole set of observer poles is positioned at $-\omega_o$ with ω_o being the observer bandwidth.

The parameters l_1 and l_2 are calculated in a manner that ensures that the matrix $A - LC$ is Hurwitz, where the genuine parts of their eigenvalues are negative.

The observer bandwidth ought to be carefully chosen as a compromise between the performance in tracking and noise resilience since a greater widening of the observer bandwidth estimates the precision while also increasing the sensitivity to noise [28].

3.2. Discussion of Overall Closed-Loop Stability

The exponential stability of extended observers allows us to use a separation principle in the study of overall closed-loop stability [29,30].

Let the tracking speed global error,

$$e_g = \omega_{ref} - \hat{\omega} \quad (19)$$

$$e_g = \underbrace{\omega_{ref} - \omega_{mes}}_{e_{(\omega)}} + \underbrace{\omega_{mes} - \hat{\omega}}_{e_1} \quad (20)$$

where ω_{ref} and $\hat{\omega}$ are a reference and the estimated speed.

$$e_g = e_{(\omega)} + e_1 \implies e_{(\omega)} = e_g - e_1 \quad (21)$$

If $e_g \rightarrow 0$ and $e_1 \rightarrow 0$, then $e_{(\omega)} \rightarrow 0$. So, with this control, we achieve the best tracking of the intended trajectory. For this, we reformulate the backstepping control procedure with e_g instead of $e_{(\omega)}$.

The derivative of Equation (19) error is,

$$\dot{e}_g = \dot{\omega}_{ref} - \dot{\hat{\omega}} \quad (22)$$

Considering the positive definite Lyapunov function $V(e_g)$,

$$V(e_g) = \frac{1}{2}e_g^2 \quad (23)$$

The time derivative of Lyapunov function is,

$$\dot{V}(e_g) = e_g \dot{e}_g \quad (24)$$

and substituting Equation (22) into Equation (24), we get

$$\dot{V}(e_g) = e_g(\dot{\omega}_{ref} - \dot{\hat{\omega}}) \quad (25)$$

The estimated time derivative speed from Equation (15) is

$$\dot{\hat{\omega}} = \frac{1}{J}(\hat{\tau}_g - \tau_{em} - f\hat{\omega}) + l_1 e_1 \quad (26)$$

and by replacing Equation (26) into Equation (25), we obtain

$$\dot{V} = e_g \left(\dot{\omega}_{ref} - \frac{1}{J}(\hat{\tau}_g - \tau_{em} - f\hat{\omega}) - l_1 e_1 \right) \quad (27)$$

The stabilisation of e_g can be produced by using a virtual control,

$$\tau_{em_{ref}} = -J\dot{\omega}_{ref} - f\hat{\omega} + \hat{\tau}_g - ke_g \quad (28)$$

where $k \in R^+$ is a real positive constant.

The control law given in Equation (18).

By substituting Equation (28) into Equation (27):

$$\dot{V} = -ke_g^2 - e_g l_1 e_1 \quad (29)$$

Since $e_1 \rightarrow 0$ exponentially, the term $(e_g l_1 e_1)$ vanishes after a short time, consequently,

$$\dot{V} = -ke_g^2 < 0 \quad (30)$$

By Equation (30), we show that $e_g \rightarrow 0$, in this case $e_{(\omega)} \rightarrow 0$.

We conclude that the control law given by Equation (28) attains accurate tracking of the intended trajectory and gives an effective FTC.

3.3. Actuator Fault Detection and Isolation

AFTC is concerned with reconfigurable control systems, which alter the control action in response to system component faults, based on real-time data on the system's current state as established by an FDI scheme. Due to their capacity to approximate any function, fuzzy inference systems (FISs) are employed to approximate nonlinear functions, uncertain or unknown.

In this study, a neurofuzzy detector and a linear transition function are used to build an FDI system to detect and isolate faulty actuators. The structure of the neurofuzzy detector is formed by integrating multiple TS FISs, by projecting data onto the components of a principal component analysis.

To isolate the actuator fault, a linear transition function is used, the linear function being a combination function between the measured torque τ_g and the estimated torque $\hat{\tau}_g$.

$$U = S\tau_g - (S - 1)\hat{\tau}_g \quad (31)$$

where S represents the state of the torque actuator, and also is the result of a neurofuzzy detector who represents the status of the actuator and can take one of the two variables F or H . F represents the faulty status of the actuator and H represents the healthy status of the actuator, where $H = 1$ and $F = 0$.

3.3.1. Neurofuzzy Detector Based on PCA Projections

The neurofuzzy detector proposed combines principal component analysis (PCA) with an adaptive neurofuzzy inference system (ANFIS). The ANFIS combines the advantages of fuzzy logic to represent knowledge in an interpretable rule-based form with linguistic labels of human language with the learning advantages of adaptive neural networks (ANNs) to optimise the antecedents and consequent parameters of fuzzy rules. With both techniques, a neurofuzzy detector is developed, which is based on two FISs to detect fault data in generator torque.

Initially, a correlation analysis of the system data is performed according to [31]. Thus, the correlation coefficient matrix of the wind turbine data was obtained $^{WT}R \in \mathbb{R}^{9 \times 9}$ with $M = 9$ variables, respectively. This analysis indicates that the variables that most interrelated with (τ_g) , which is the variable of interest, are those with a Pearson’s correlation coefficient of $\rho \geq 0.98$. Figure 2 depicts the matrix of correlation coefficients of the wind turbine data.

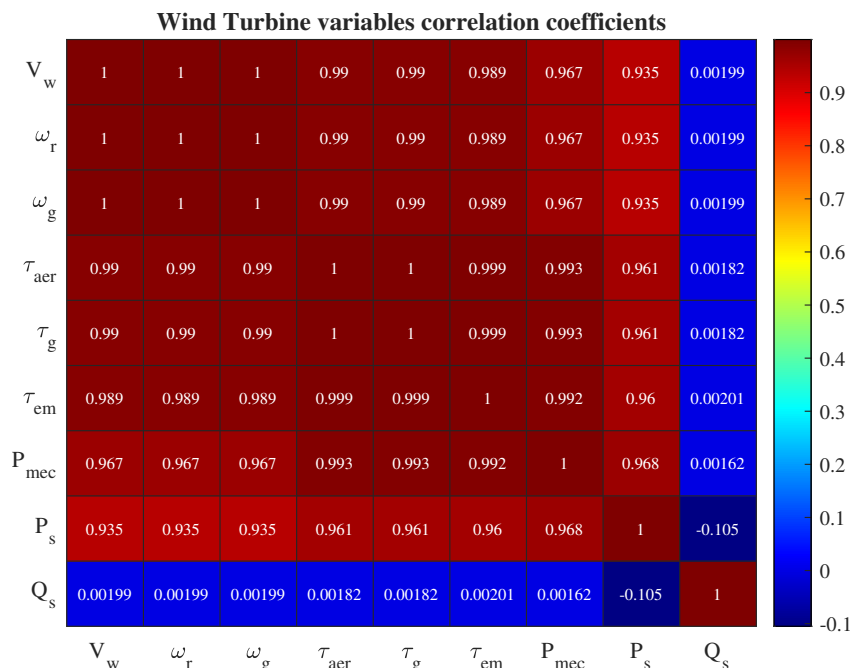


Figure 2. Correlation coefficient matrix of the wind turbine.

The neurofuzzy detector uses the input variables shown in Figure 3, which are the result of the analysis presented previously: wind speed (V_w), generator torque (τ_g), aero-generator torque (τ_{aer}), and electromagnetic torque (τ_{em}).

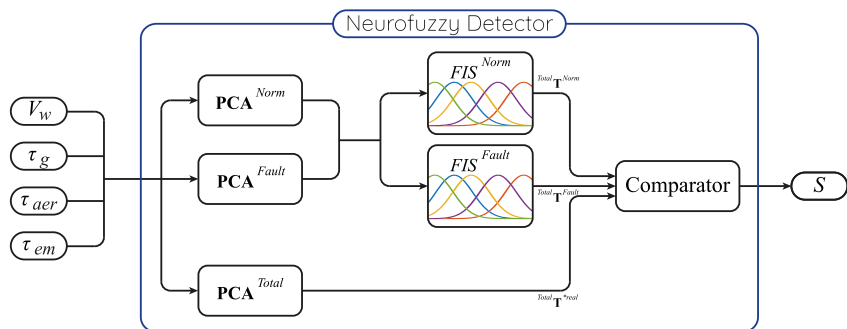


Figure 3. Structure of the neurofuzzy detector.

3.3.2. Projection of Data on Principal Components

Subsequently, data groups are formed in normal operation (*Normal*), faulty operation (*Fault*) that contains fault data on τ_g , and a total group (*Total*) grouping the normal and faulty operation data.

As presented in [32], a PCA is implemented offline for each data set, acquiring a covariance matrix PCA^s generally referred to as the load matrix, that contains the eigenvectors v_r of the eigenvalues λ_r and indicates the orientation of the updated principal component (PC) space. It is used to reduce the dimensional of the variable space by projecting the original data using Equation (32).

$$\text{Norm}\mathbf{T}^s = \mathbf{Z}^{\text{Norm}} \times \mathbf{PCA}^s \quad (32a)$$

$$\text{Fault}\mathbf{T}^s = \mathbf{Z}^{\text{Fault}} \times \mathbf{PCA}^s \quad (32b)$$

$$\text{Total}\mathbf{T}^s = \mathbf{Z}^s \times \mathbf{PCA}^{\text{Total}} \quad (32c)$$

where \mathbf{Z}^s is a matrix that contains normalised data for each group $s \rightarrow \{\text{Norm}, \text{Fault}\}$ and \mathbf{T}^s is the matrix of scores for each s , which consists of a new component mapped on its corresponding PC.

Typically, the matrix of data is mapped onto the element that consists of the greatest variation, and the new projected variables exhibit no correlation, as noted in [33]. In this case, for normal operation data, the first PC represents a variability of 99.61%, for faulty operation data the first PC represents a variability of 95.61%, and for both groups the first PC represent a variability of 96.87%. Therefore, the projection of each data group is performed on the first PC and these projections are used in the learning process of the ANFIS. The learning data set (80%) and validation data set (20%) are created with the projected data. In addition, training (70%) and checking (30%) sets are formed from the learning data as follows:

$$\text{Norm}\mathbf{T}_{\text{rn}} = \begin{bmatrix} \text{Norm}\mathbf{T}^{\text{Norm}} & \text{Norm}\mathbf{T}^{\text{Fault}} & \text{Total}\mathbf{T}^{\text{Norm}} \end{bmatrix}, \quad (33a)$$

$$\text{Fault}\mathbf{T}_{\text{rn}} = \begin{bmatrix} \text{Fault}\mathbf{T}^{\text{Norm}} & \text{Fault}\mathbf{T}^{\text{Fault}} & \text{Total}\mathbf{T}^{\text{Fault}} \end{bmatrix}, \quad (33b)$$

As can be appreciated, the projection of each group on the other groups forms the training set. The checking and validation sets were obtained following the same procedure.

3.3.3. Learning Process of the Detector

The structure of the neuro-fuzzy detector is composed of two FISs, which were obtained from the training procedure of two ANFIS networks. Each ANFIS network [34] uses training and checking sets to capture the behaviour of the fault in the learning process. In this process, the ANFIS looks at the normalised RMSE of the training set and the check set to not overfit only the first set, which would cause the obtained FIS to output inappropriate values for values that have not been seen in the learning process. In this way, it seeks a middle ground where learning is general in both groups according to [32].

The training of each ANFIS is executed by first employing the method based on clustering (subtractive grouping) [35] to estimate both the quantity and initial centers of the Gaussian membership functions (MF) utilised in the fuzzy rules. Afterward, the elements of each ANFIS layer are refreshed employing a hybrid training method, which combines gradient descent to acquire the elements that determine the MF of each fuzzy set *antecedent parameters* and minimises the squared difference to determine the coefficients of every first-order polynomial function, referred to as the resulting linear parameters for each epoch or sweep. The elements of the ANFIS structure are shown in Table 1.

Table 1. ANFIS parameters

Description	ANFIS	
Type of MF	Gaussian	
Method of optimisation:	Hybrid	
Type of MF output:	Linear	
FIS	<i>Norm</i>	<i>Fault</i>
MFs number:	3	3
Rules number:	3	3
The range of influence	0.7	0.7
The number of the epoch:	1500	1500

Once the ANFIS learning process has been completed, FIS^{Norm} and FIS^{Fault} are obtained, which estimate the behaviour of faults in τ_g . Both FIS contains three Takagi–Sugeno type rules as the following:

$$\text{IF } x_1 \text{ is } F_{1j} \text{ and } x_2 \text{ is } F_{2j} \text{ and } x_i \text{ is } F_{ij},$$

$$\text{THEN : } f_j(x) = g_{0j} + g_{1j}x_1 + \dots + g_{ij}x_i$$

where the description of each of the parameters that make up the rule is extensively described in [31].

The failure in τ_g is determined through the output of each FIS^s which is the projection of the detector input data set $D^{in} = [V_w \ \tau_g \ \tau_{aer} \ \tau_{em}]$ onto the first PC in the total group ($Total\mathbf{T}^s$). A comparator block, as shown in Figure 3, is then used, which consists of an Exhaustive Search Algorithm (ESA) and a rule. The ESA is composed of a cost function that defines which FIS^s attains the actual projection $Total\mathbf{T}^{*real}$ of a new incoming data set by direct evaluation, choosing the FIS that minimises the cost function. The FIS^s that presents the minimum $J^s \rightarrow \{J^{Norm} \in 1, J^{Fault} \in 2\}$ sets the group to which the updated data set (D^{in}) is associated.

$$J^s = \left\| Total\mathbf{T}^{*real} - Total\mathbf{T}^s \right\|_2^2 \quad (34)$$

Finally, the rule determines if τ_g fails or not in the follows

$$\text{IF } J^s = 1 \text{ THEN } S = 0 \text{ ELSE } S = 1$$

where $S = 0$ represents the healthy status of the actuator and $S = 1$ represents the faulty status of the actuator.

3.3.4. Evaluation of the Detector

The evaluation process consists of testing the neurofuzzy detector with validation data. Both FIS^s are evaluated with the data of each group. If new input data (D^{in}) do not contain a fault in τ_g , the output of FIS^{Norm} is closer to the actual projection $Total\mathbf{T}^{*real}$. On the other hand, if D^{in} contains failures in τ_g , the output of FIS^{Fault} is closer to the actual projection ($Total\mathbf{T}^{*real}$).

The evaluation process compares the output of FIS^s with the validation data set, that is, the new data set's input–output samples. Thus, the error indexes were used to compare the FIS^s outputs ($Total\mathbf{T}^s$) with the actual output data ($Total\mathbf{T}^{*real}$) according to [33]. The arithmetic error mean (\bar{E}), standard deviation (Std), Root Mean Square Error ($RMSE$), and the coefficient of determination R^2 provide information about precision, i.e., how much the error is dispersed, and are presented in Table 2.

Table 2. Validation index of FIS^s .

Error	Neurofuzzy Models	
Indexes	FIS^{Norm}	FIS^{Fault}
\bar{E}	0.18×10^{-6}	0.034×10^{-6}
Std	$\pm 1.28 \times 10^{-6}$	$\pm 21.02 \times 10^{-6}$
$RMSE$	1.30×10^{-6}	21.01×10^{-6}
R^2	0.9999	0.9999

The proposed comparator block determines if there is a failure or not in τ_g . In this block, ESA conducts a direct evaluation by comparing the cost function J^s with the estimate projection value ($Total\mathbf{T}^s$) of each FIS^s and allocates the value of the tag $\{J^{Norm} \in 1, J^{Fault} \in 2\}$ that minimises this function. Subsequently, the rule determines the fault and assigns the corresponding value to S .

If the evaluated data (D^{in}) are of normal operation, the FIS^{Norm} will minimise the cost function and that group is assigned to the data, while the rule will determine the existence of a fault, as shown in Figure 4.

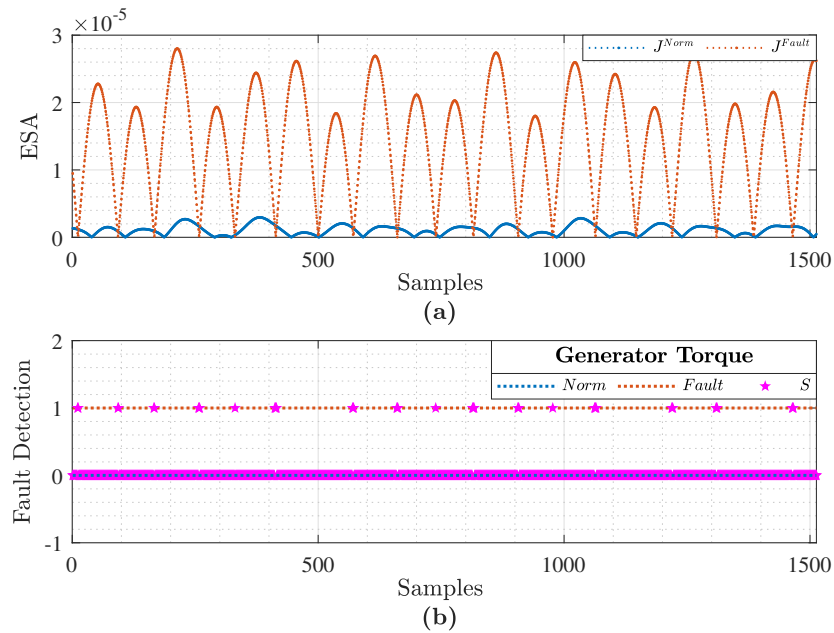


Figure 4. NF detector testing with normal operation data. (a) Error obtained from direct comparison in the ESA between $Total\ T^{Norm}$ and $Total\ T^{*real}$. (b) Fault detection process.

Figure 5 shows that when (D^{in}) has a faulty operation, the FIS^{Fault} will minimise the cost function and that group is allocated to the data. In the same way, the rule determine the existence of a fault.

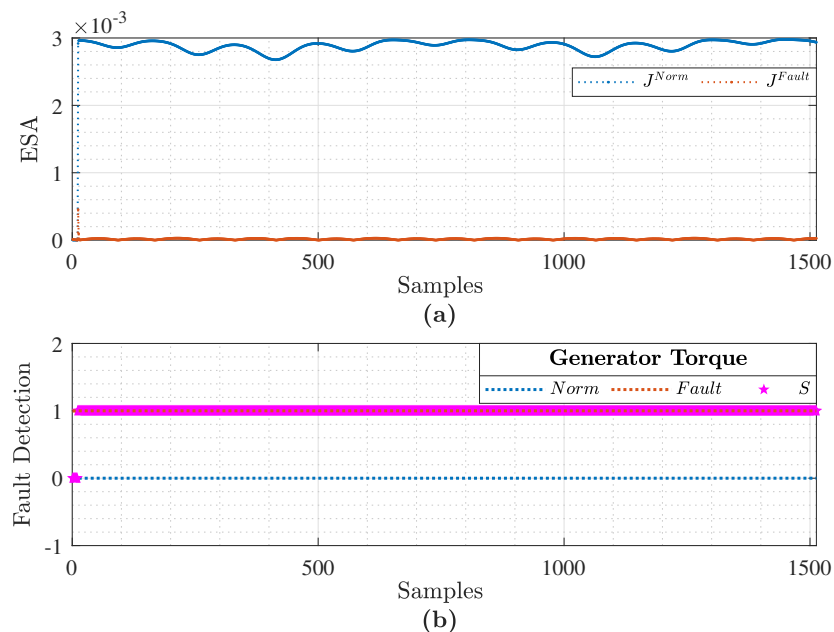


Figure 5. NF detector testing with faulty operation data. (a) Error obtained from direct comparison in the ESA between $Total\ T^{Fault}$ and $Total\ T^{*real}$. (b) Fault detection process.

Furthermore, a confusion matrix (see Table 3) has been constructed to evaluate the proposed detector; this matrix shows the dispersion of the groups attributed to the predicted data, assigned to their true groups.

Table 3. Confusion matrix τ_g .

		Predicted	
		Normal	Fault
Actual	Normal	1471	42
	Fault	10	1503
	Precision	97.22%	99.34%
	Recall	99.33%	
	Accuracy	98.28%	

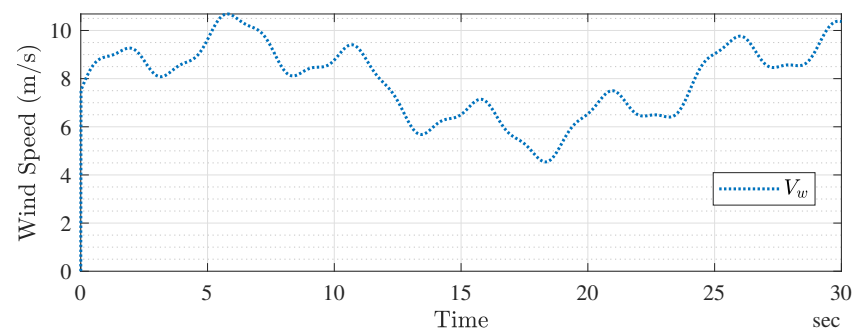
4. Simulation Result

In order to evaluate the efficacy of the proposed technique, we developed a wind turbine simulation with a variable power conversion system in MATLAB/Simulink software 2021b package with sampling time $T_s = 10^{-2}$ s. The FTC with and without fault diagnosis and isolation was studied introducing the actuator fault as an offset in generator torque at $t = 15$ s. Table 4 contains the wind turbine and generator parameters.

Table 4. Parameters of the wind turbine and generator [36].

Wind Turbine Parameters	Value
Power rate P_n (kW)	10
Density of the air ρ (kg/m ³)	1.225
Number of blades	3
Rotor radius R (m)	3
Ratio of the gearbox ratio N_g	5.4
Total Inertia of the turbine J (kg·m ²)	0.02
Coefficient of the total viscous friction B (Nm/s)	0.0016
Generator Parameters	Value
Nominal Power P_n (kW)	10
Number of poles pair p	2
Nominal Speed (rpm)	1440
Rotor resistance R_r (Ω)	0.62
Stator resistance R_s (Ω)	0.455
Rotor inductance L_r (mH)	0.081
Stator inductance L_s (mH)	0.084
Mutual inductance Rotor/Stator M (mH)	0.02661

The wind profile is presented in Figure 6, which reveals that the speed fluctuates by roughly 10% between 0 and 30 s.

**Figure 6.** Wind profile.

Three scenarios were considered that are discussed in the following subsections.

4.1. Scenario 1

In this scenario, a fault of 30% from the measured value was created without the FTC controller in order to show the influence of the faulty actuator generator torque on the wind turbine performance.

Figure 7 suggests that a fault in the actuator generator torque has a substantial influence on the performance of the mechanism. The simulation outcomes indicate that when the fault occurred at time 15 s, a 30% loss in the nominal torque value resulted, from 23.5 Nm to 16 Nm, as depicted in Figure 7a. As a result of this fault, there was an increase in the generator speed from 108 rd/s to 111 rd/s, as shown in Figure 7b.

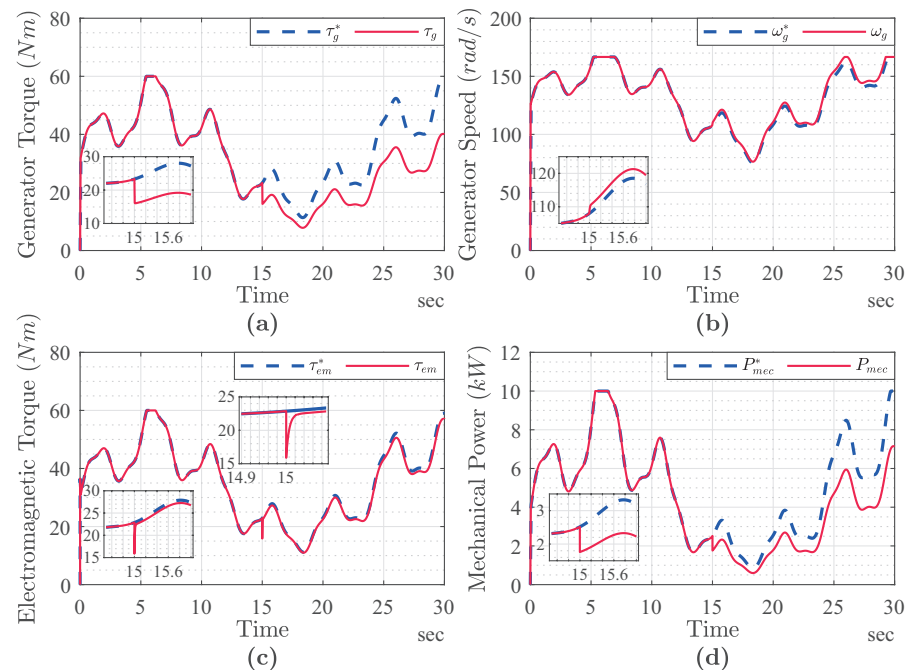


Figure 7. Wind turbine mechanical performance under a generator actuator fault without AFTC (a). Generator torque (b) generator speed, (c) electromagnetic torque, (d) mechanical power.

The MPPTs electromagnetic torque output decreased from the nominal value of 23.5 Nm to 16 Nm, and although the backstepping controller was implemented to correct the perturbation, there remained a 0.5 Nm difference from the nominal value, as seen in Figure 7c. The decrease in generator actuator torque led to a reduction in mechanical power, which dropped from the nominal value of 2.5 kW to 1.7 kW due to the relationship between generator torque and speed, as presented in Figure 7d.

The mechanical power serves as the reference electrical power for the generator, as demonstrated in Figure 8a,b. The fault caused a decrease in the rotor and stator currents from the nominal values, as revealed in Figure 8c,d, due to the decrease in reference power involved in the generator actuator fault.

Overall, the simulation results provide valuable insights into the system's performance under failure conditions. The results underscore the requirement for fault-tolerant control mechanisms that can help the system maintain its performance even under fault conditions.

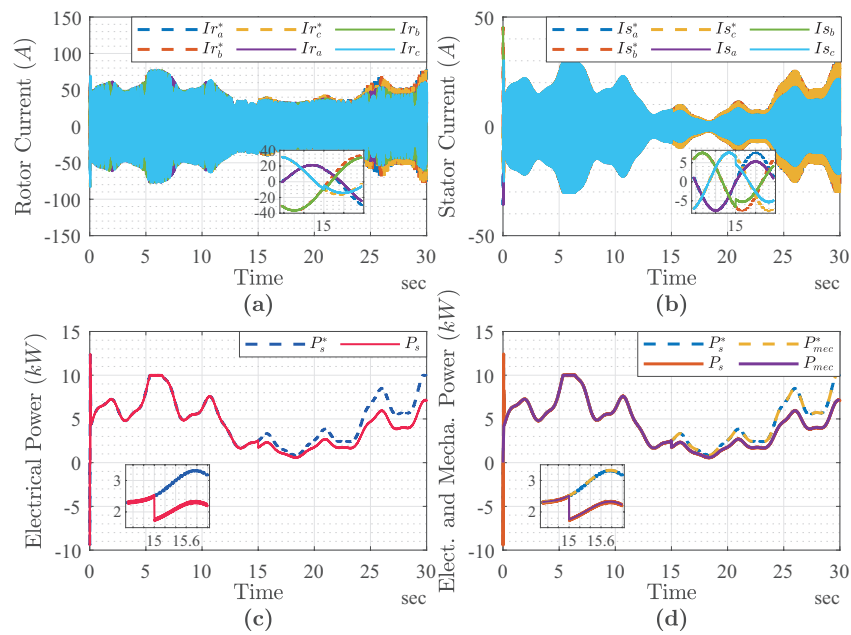


Figure 8. Wind turbine electrical performance under a generator actuator fault without AFC. (a) Generator torque, (b) generator speed, (c). electromagnetic torque, (d) mechanical power.

4.2. Scenario 2

The aim of this scenario is to apply the FTC based on the BADRC after 5 s with a manual isolation switch by a local operator between the failed actuator torque and the estimated torque to show how the FTC enhances the performance of the wind turbine.

The manual transition from the failed generator actuator torque to the estimated one delivered by the FTC controller in improving the performance of the system is shown in Figure 9. Due to the architecture of the observer, switching between the faulty value of torque and the observed one will improve the estimated value to join the nominal, as illustrated in Figure 9a. As a result, the generator speed will decrease to join the nominal value as shown in Figure 9b.

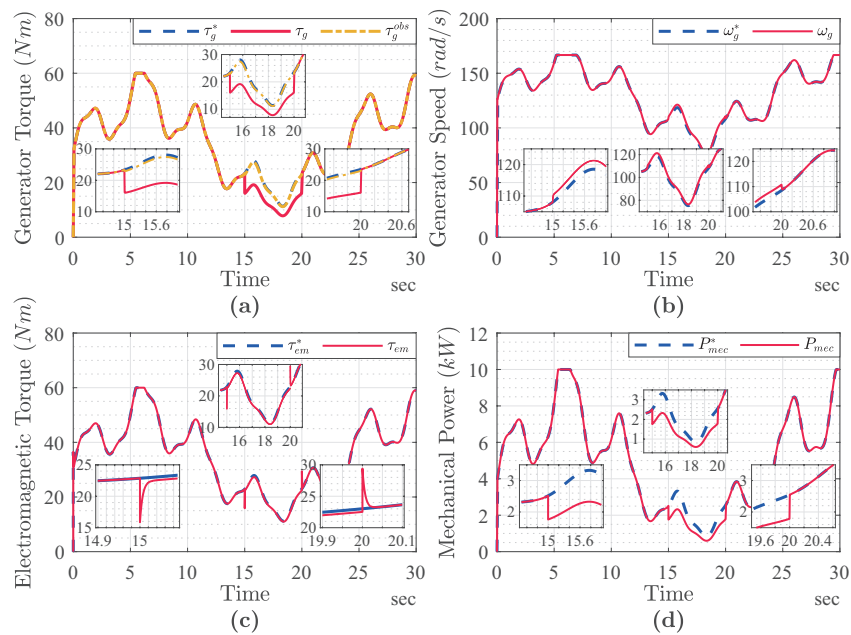


Figure 9. Wind turbine mechanical performance under a generator actuator fault with FTC. (a) Generator torque, (b) generator speed, (c) electromagnetic torque, (d) mechanical power.

The MPPTs electromagnetic torque outcomes increased to the nominal value, suppressing the 0.5 Nm effect of the fault, as seen in Figure 9c. The FTC observer torque led to a growth in mechanical power, which lifted to the nominal value due to the relationship between generator torque and speed, as presented in Figure 9d.

As demonstrated in Figure 10a,b, the mechanical power is the reference electrical power for the generator. The FTC correction caused an increase in the rotor and stator currents to join the nominal values, as illustrated in Figure 10c,d, due to the growth in electrical reference power involved in the FTC observed value of the generator torque.

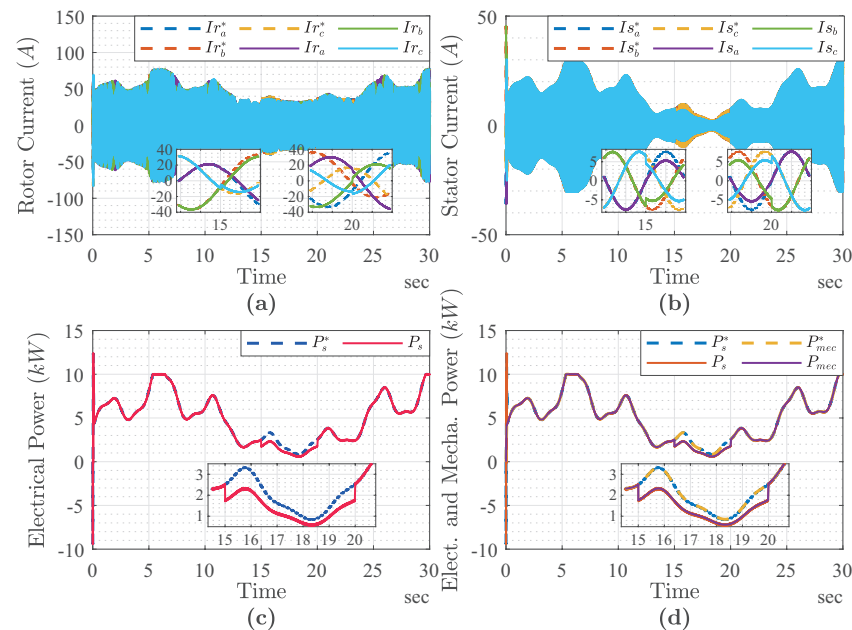


Figure 10. Wind turbine electrical performance under a generator actuator fault with FTC. (a) Rotor currents, (b) stator currents, (c) electrical power, (d) mechanical and electrical power.

4.3. Scenario 3

In this scenario, the control phases of the wind turbine are managed autonomously via the detector ANFIS isolation switch from the failed actuator torque to the observed one.

The evaluated data (D^{in}) contain normal and faulty data. Figure 11 shows the estimate projection ($Total \mathbf{T}^s$) by each FIS and real projection $Total \mathbf{T}^{*real}$. As can be appreciated in Figure 11a, the output of FIS^{Norm} is closer to the actual projection $Total \mathbf{T}^{*real}$, while Figure 11b shows that the output of FIS^{Fault} is closer to the actual projection $Total \mathbf{T}^{*real}$.

In the comparator block, the ESA will minimise the cost function J^s and that group is assigned to the data, while the rule will determine the existence of failure or not, as shown in Figure 12. In addition, the results of this scenario are shown by a confusion matrix in Table 5, which indicates good results in the detection of τ_g .

The results of the confusion matrix in Table 5 demonstrate the high performance of the model in detecting false data in torque. The precision of the true class, which represents the accuracy in detecting real data, was 90.20%, indicating that most true data samples were correctly identified. Furthermore, the precision for the false class, which indicates the accuracy in detecting false data, was 100%, signifying that all false data samples were correctly identified.

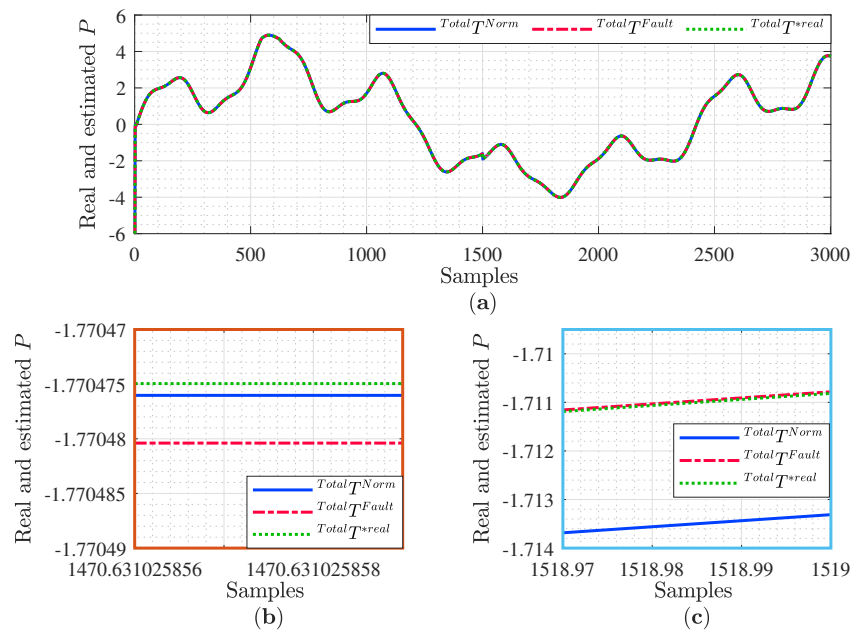


Figure 11. The output of each FIS. (a) The whole estimated values of the projection $Total T^s$. (b) Zoom in of a section where the input data to the detector are not faulty. (c) Zoom in on a section where the input data to the detector are faulty.

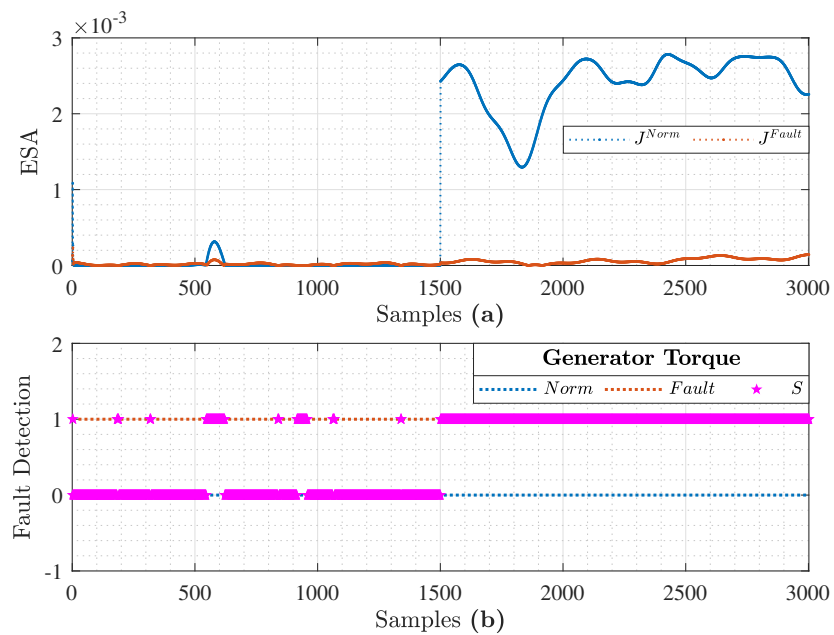


Figure 12. NF detector testing with normal and faulty operation data. (a) Error obtained from direct comparison in the ESA between $Total T^s$ and $Total T^{*real}$. (b) Fault detection process.

The recall, which represents the ability of the model to detect all false data, was 100%, indicating that there were no false negatives in the detection process.

In general, the model achieved an accuracy of 95.10%, which means that 95.10% of the data samples were correctly classified as true or false. These results demonstrate a robust performance of the model in detecting false data in torque, which is crucial for ensuring the accuracy and reliability of data in torque-related applications.

Table 5. Confusion matrix τ_g for scenario 3.

		Predicted	
		Normal	Fault
Actual	Normal	1354	147
	Fault	0	1501
Precision		90.20%	100%
Recall		100%	
Accuracy		95.10%	

Table 6 presents the results of the neurofuzzy false data detector. Two groups were evaluated: “Normal” and “Fault”. For the “Normal” group, 1354 out of 1501 actual samples were correctly predicted. However, 147 false data were erroneously classified as faults within the “Normal” group. On the other hand, all 1501 samples in the “Fault” group were correctly predicted, and no false data were identified. Overall, of the 3002 total samples evaluated, 147 were mistakenly classified as faults. These findings indicate that the unreliable data detector performs well in fault detection, but there is a need for improvement in accurately classifying normal data as nonfaults.

Table 6. Results of the NF detector.

Group	Electromagnetic Torque			
	Predicted	Actual	False Normal	False Fault
Normal	1354	1501	0	147
Fault	1501	1501	0	0
Total samples	3002	3002	0	147

The entire process incurs a computational burden time of 2.6193 seconds (see Table 7), with each individual sample demanding a remarkably brief duration of approximately 0.873×10^{-3} . Furthermore, the first ANFIS model achieved a training nRMSE of 8.157×10^{-6} and a checking nRMSE of 8.625×10^{-6} , whereas the second ANFIS model exhibited even higher precision, boasting a training nRMSE of 0.281×10^{-6} and a checking nRMSE of 0.2908×10^{-6} .

Table 7. Computational complexity of the algorithm.

ANFIS Type	Inputs	MF Type	MFs	Ant. Param.	Total Rules	Consq Param.	Total Param.	Trn nRMSE	Chk nRMSE
Type 3	4	Gaussian	3	9	3	12	21	8.157×10^{-6}	8.625×10^{-6}
Type 3	4	Gaussian	3	9	3	12	21	0.281×10^{-6}	0.2908×10^{-6}
Computational Burden				Time per sample (s)			Total Time (s)		
				0.873×10^{-3}			2.6193		

Despite the negative effects of the defect, Figures 13 and 14 demonstrate that the proposed AFTC controller based on BADRC theory and the adaptive neurofuzzy isolation makes the process more efficient and drives the system to extract the greater amount of power without perturbing any mechanical and electrical performances.

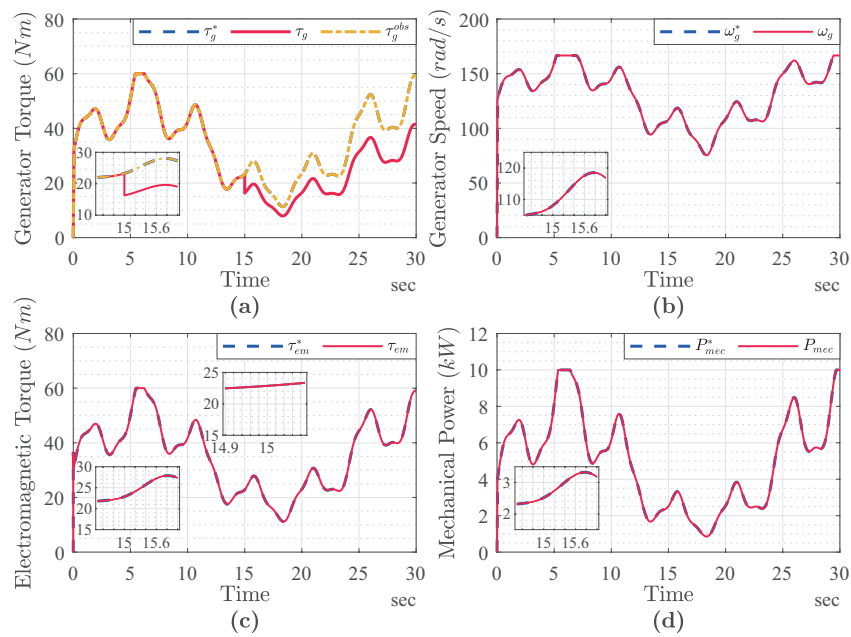


Figure 13. Wind turbine mechanical performance under generator actuator fault with AFTC. (a) Generator torque, (b) generator speed, (c) electromagnetic torque, (d) mechanical power.

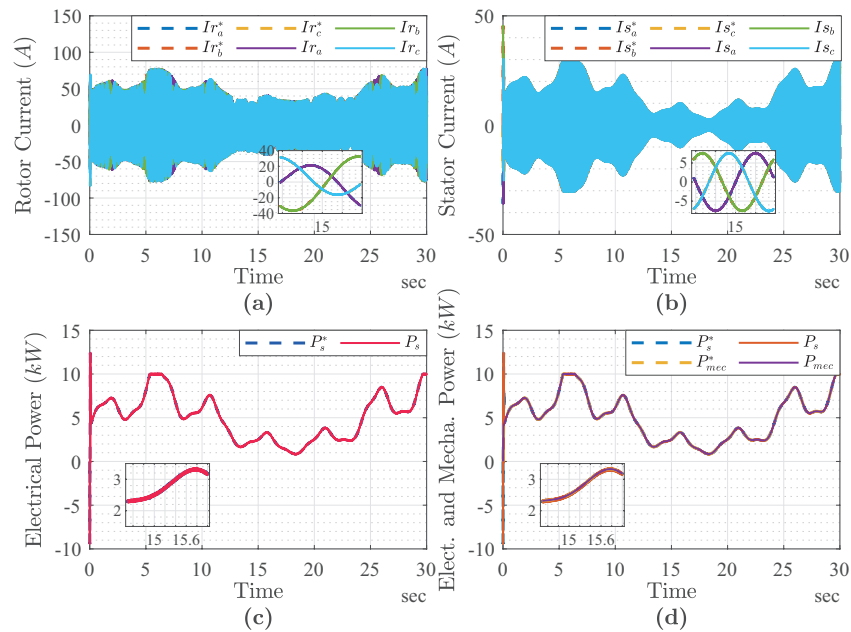


Figure 14. Wind turbine electrical performance under generator actuator fault with AFTC. (a) Rotor currents, (b) stator currents, (c) electrical power, (d) mechanical and electrical power.

To gain insight into the effectiveness of the proposed method, a comparison is made with various fault detection and isolation (FDI) methods. The work carried out in [14] presents a fault detection approach of τ_g failure as the increasing offset in generator torque (f_9); the author defines the diagnosis time (T_D) in terms of the sampling time ($T_s = 12.5$ ms). The proposed method in this manuscript uses a sampling time $T_s = 10$ ms for a simulation of 30 s (3002 samples), and the fault occurs at 15 s (see Figure 13). The effectiveness of the proposed method in this manuscript is compared in the same way as in [14] and is shown in Table 8. As we can observe, the proposed method is much faster compared to the other methods.

Table 8. Comparison of the proposed method with other methods in terms of diagnosis time.

Fault	T_D (ms) Required	T_D (ms) Obtained						
		Detector	qLPVZO	TSIO	ANNK	SVMKF	RSVM	MBIO
τ_g	$T_D < 37.5$	0.873	12.5	25	225	437.5	37.5	37.5

5. Conclusions

The simulation results illustrate the efficiency of the suggested approach in addressing the actuator generator torque failure problem while also isolating the faulty actuator. The neurofuzzy detector demonstrates exceptional capability in identifying erroneous torque data, exhibiting remarkable precision rates of 90.20% for real data and 100% for false data. It achieves a perfect recall score of 100%, signifying the absence of false negatives. Moreover, the overall precision of 95.10% serves as a testament to the detector's consistent aptitude in accurately categorising data as true or false. Furthermore, the computational burden time for the entire process is 2.6193 s, with each individual sample requiring an impressively short time of approximately 0.873×10^{-3} . Moreover, the first ANFIS model achieved a training nRMSE of 8.157×10^{-6} and a checking nRMSE of 8.625×10^{-6} , while the second ANFIS model demonstrated even greater precision with a training nRMSE of 0.281×10^{-6} and a checking nRMSE of 0.2908×10^{-6} . These compelling findings firmly emphasise the resilience of the detector to detect false data, thus guaranteeing the highest accuracy and dependability in the specific application at hand.

Furthermore, the results demonstrate that the utilisation of BADRC and neurofuzzy isolation presents a dependable and resilient solution to tackling the problem of actuator generator torque failure. This approach not only maximises power extraction, but also effectively mitigates the risk of additional damage. In summary, the study emphasises the potential of BADRC and ANFIS detection and isolation as a promising strategy to enhance the reliability and performance of wind energy conversion systems, specifically in offshore wind farms. As part of future work, the investigation will extend to failures that occur under varying forces, including the exploration of simultaneous failures.

Highlighting the challenges and limitations of the proposed algorithm, the proposed method is designed to detect only generator actuator failures and ANFIS for normal operation; sometimes, it may misclassify data as failures. In future work, this method will be extended and improved to detect various faults and improve the above points by using the genetic algorithm to determine the parameters of the membership function parameters.

Author Contributions: Conceptualization, H.A.; Methodology, H.A., W.D.C. and A.K.; Software, H.A., W.D.C. and A.K.; Validation, H.A.; Formal analysis, H.A.; Investigation, H.A., W.D.C. and A.K.; Resources, H.A., H.M.B. and J.M.E.; Writing—original draft, H.A., W.D.C. and A.K.; Writing—review & editing, H.M.B., J.M.E., J.L.M.-R. and M.D.; Visualization, H.A. and W.D.C.; Supervision, H.M.B., J.M.E., J.L.M.-R. and M.D. All authors have read and agreed to the published version of the manuscript.

Funding: This research received no external funding.

Data Availability Statement: Not applicable.

Acknowledgments: The authors would like to thank the editors and anonymous reviewers for providing insightful suggestions and comments to improve the quality of research paper. The first author would also like to acknowledge the financial support of the Erasmus+ program for research periods at the University of Seville. The authors also would like to thank the European Union for support this work under DENiM project. This project has received funding from the European Union's Horizon 2020 research and innovation program under grant agreement No 958339.

Conflicts of Interest: The authors declare no conflict of interest.

Abbreviations

The following abbreviations and variables are used in this manuscript:

AFTC	Active Fault Tolerant Control
BADRC	Backstepping Active Disturbance Rejection Control
ANFIS	Adaptive Neurofuzzy Inference System
SDGs	Sustainable Development Goals
PCA	Principal Component Analysis
MPPT	Maximum Power Point Tracking
FTC	Fault Tolerant Control
FIS	Fuzzy Inference System
FDI	Fault Detection and Isolating
SVM	Support Vector Machine
DNN	Deep Neural Networks
ARRs	Analytical Redundancy Relations
TS	Takagi–Sugeno
qLPV	quasi-Linear Parameter Varying
HSS	High Speed Shaft
LSS	Low Speed Shaft
DFIG	Double Fed Induction Generator
FIS	Fuzzy Inference System
ESA	Exhaustive Search Algorithm
ANNs	Adaptive Neural Networks
RMSE	Root Mean Square Error
TSIO	Takagi–Sugeno Interval Observer
ANNK	Artificial Neural Networks and k-Nearest Neighbors
SVMKF	Support Vector Machine and Kalman Filter
RSVM	Residual Support Vector Machine
MBIO	Model-Based Interval Observer

Variables

P_{aer}	Aerodynamic Power
R	The Rotor Radius
V_w	The Wind Speed
C_p	The Power Coefficient
λ	The Tip Speed Ratio
β	The Blade Pitch Angle
ω_t	The Shaft's Angular Velocity
$C_{p_{max}}$	The Highest Value of The Power Coefficient
λ_{opt}	The Optimal Value of The Tip Speed Ratio
$\omega_{t_{opt}}$	The Optimal Value of The Shaft's Angular Velocity
N_g	Ratio of The Gearbox
ω_g	The Generator Speed
$\tau_t, \tau_g, \tau_{em}$	The Turbine, Generator and Electromagnetic Torque
J	The Total Inertia
J_t, J_g	The Turbine Inertia and The Generator Inertia
ω_{mes}	The Measured Shaft's Angular Velocity
V_{sd}, V_{sq}	The d/q Stator Voltages
V_{rd}, V_{rq}	The d/q Rotor Voltages
I_{sd}, I_{sq}	The d/q Stator Currents
I_{rd}, I_{rq}	The d/q Rotor Currents
ϕ_{sd}, ϕ_{sq}	The d/q Flux Currents
ϕ_{rd}, ϕ_{rq}	The d/q Flux Currents
R_s, R_r	The Stator and Rortor Resistance
L_s, L_r	The Stator and Rortor Inductance
M	The Magnetising Inductance
ω_s, ω_r	The Stator and Rotor Electrical Speed
$-\omega_0, \omega_0$	The Observer Bandwidth.
P_g	The Generator Power

f	The Generator Viscous Friction Coefficient
S	The Output of The Detector
H, F	The Healthy Status of The Actuator and The Faulty Status of The Actuator
f_g	The Fault of Generator Torque
T_s, T_D	The Sampling Time and The Diagnosis Time

References

- Mauricio, J.M.; Marano, A.; Gomez-Exposito, A.; Martinez Ramos, J.L. Frequency Regulation Contribution Through Variable-Speed Wind Energy Conversion Systems. *IEEE Trans. Power Syst.* **2009**, *24*, 173–180. [[CrossRef](#)]
- Sarkar, D.; Shukla, S.; Alom, N.; Sharma, P.; Bora, B.J. Investigation of a Newly Developed Slotted Bladed Darrieus Vertical Axis Wind Turbine: A Numerical and Response Surface Methodology Analysis. *J. Energy Resour. Technol.* **2022**, *145*, 051302. [[CrossRef](#)]
- Fathabadi, H. Novel high-efficient unified maximum power point tracking controller for hybrid fuel cell/wind systems. *Appl. Energy* **2016**, *183*, 1498–1510. [[CrossRef](#)]
- Sarfejo, M.D.; Dehchil, M.N.; Jelodar, S.R. MPPT Approach for Fixed Speed wind Turbine by Using Proportional-Integral Controller. In Proceedings of the 2019 27th Iranian Conference on Electrical Engineering (ICEE), Yazd, Iran, 30 April–2 May 2019; pp. 598–601. [[CrossRef](#)]
- Kamal, E.; Aitouche, A.; ABBES, D. Robust fuzzy scheduler fault tolerant control of wind energy systems subject to sensor and actuator faults. *Int. J. Electr. Power Energy Syst.* **2014**, *55*, 402–419. [[CrossRef](#)]
- Zhang, Y.; Jiang, J. Bibliographical review on reconfigurable fault-tolerant control systems. *Annu. Rev. Control.* **2008**, *32*, 229–252. [[CrossRef](#)]
- Sheibat-Othman, N.; Othman, S.; Benlahrache, M.; Odgaard, P.F. Fault detection and isolation in wind turbines using support vector machines and observers. In Proceedings of the 2013 American Control Conference, Washington, DC, USA, 17–19 June 2013; pp. 4459–4464. [[CrossRef](#)]
- Zeng, J.; Lu, D.; Zhao, Y.; Zhang, Z.; Qiao, W.; Gong, X. Wind turbine fault detection and isolation using support vector machine and a residual-based method. In Proceedings of the 2013 American Control Conference, Washington, DC, USA, 17–19 June 2013; pp. 3661–3666.
- Wen, X.; Xu, Z. Wind turbine fault diagnosis based on ReliefF-PCA and DNN. *Expert Syst. Appl.* **2021**, *178*, 115016. [[CrossRef](#)]
- Sanchez, H.; Escobet, T.; Puig, V.; Odgaard, P.F. Fault diagnosis of an advanced wind turbine benchmark using interval-based ARRs and observers. *IEEE Trans. Ind. Electron.* **2015**, *62*, 3783–3793. [[CrossRef](#)]
- Qin, H.; Tan, P.; Chen, Z.; Sun, M.; Sun, Q. Deep reinforcement learning based active disturbance rejection control for ship course control. *Neurocomputing* **2022**, *484*, 99–108. [[CrossRef](#)]
- Pérez-Pérez, E.J.; López-Estrada, F.R.; Puig, V.; Valencia-Palomo, G.; Santos-Ruiz, I. Fault diagnosis in wind turbines based on ANFIS and Takagi–Sugeno interval observers. *Expert Syst. Appl.* **2022**, *206*, 117698. [[CrossRef](#)]
- Gopi, A.; Sharma, P.; Sudhakar, K.; Ngui, W.K.; Kirpichnikova, I.; Cuce, E. Weather Impact on Solar Farm Performance: A Comparative Analysis of Machine Learning Techniques. *Sustainability* **2023**, *15*, 439. [[CrossRef](#)]
- Pérez-Pérez, E.J.; Puig, V.; López-Estrada, F.R.; Valencia-Palomo, G.; Santos-Ruiz, I.; Samada, S.E. Fault detection and isolation in wind turbines based on neuro-fuzzy qLPV zonotopic observers. *Mech. Syst. Signal Process.* **2023**, *191*, 110183. [[CrossRef](#)]
- Borja-Jaimes, V.; Adam-Medina, M.; García-Morales, J.; Guerrero-Ramírez, G.V.; López-Zapata, B.Y.; Sánchez-Coronado, E.M. Actuator FDI Scheme for a Wind Turbine Benchmark Using Sliding Mode Observers. *Processes* **2023**, *11*, 1690. [[CrossRef](#)]
- Badihi, H.; Zhang, Y.; Hong, H. Wind Turbine Fault Diagnosis and Fault-Tolerant Torque Load Control Against Actuator Faults. *IEEE Trans. Control. Syst. Technol.* **2015**, *23*, 1351–1372. [[CrossRef](#)]
- Bustan, D.; Moodi, H. Adaptive Interval Type-2 Fuzzy Controller for Variable-speed Wind Turbine. *J. Mod. Power Syst. Clean Energy* **2022**, *10*, 524–530. [[CrossRef](#)]
- Ouari, K.; Belkhier, Y.; Djouadi, H.; Kasri, A.; Bajaj, M.; Alsharef, M.; Elattar, E.E.; Kamel, S. Improved nonlinear generalized model predictive control for robustness and power enhancement of a DFIG-based wind energy converter. *Front. Energy Res.* **2022**, *10*, 996206. [[CrossRef](#)]
- Qais, M.H.; Hasanién, H.M.; Alghuwainem, S. Whale optimization algorithm-based Sugeno fuzzy logic controller for fault ride-through improvement of grid-connected variable speed wind generators. *Eng. Appl. Artif. Intell.* **2020**, *87*, 103328. [[CrossRef](#)]
- Bakhtiari, F.; Nazarzadeh, J. Optimal Estimation and Tracking Control for Variable-speed Wind Turbine with PMSG. *J. Mod. Power Syst. Clean Energy* **2020**, *8*, 159–167. [[CrossRef](#)]
- Abdeddaim, S.; Betka, A. Optimal tracking and robust power control of the DFIG wind turbine. *Int. J. Electr. Power Energy Syst.* **2013**, *49*, 234–242. [[CrossRef](#)]
- Loucif, M.; Boumédiène, A. Modeling and direct power control for a DFIG under wind speed variation. In Proceedings of the 2015 3rd International Conference on Control, Engineering & Information Technology (CEIT), Tlemcen, Algeria, 25–27 May 2015; pp. 1–6. [[CrossRef](#)]
- Tiwari, R.; Babu, N.R.; Padmanaban, S.; Martirano, L.; Siano, P. Coordinated DTC and VOC control for PMSG based grid connected wind energy conversion system. In Proceedings of the 2017 IEEE International Conference on Environment and Electrical Engineering and 2017 IEEE Industrial and Commercial Power Systems Europe (EEEIC/I&CPS Europe), Milan, Italy, 6–9 June 2017; pp. 1–6. [[CrossRef](#)]

24. Diallo, M.O.S.; Camara, M.B.; Youssef, S.; Gualous, H.; Dakyo, B. Génératrice Asynchrone à Double Alimentation pour la production d'énergie hydrolienne dans le Raz Blanchard- Modélisation et Simulations. 2014. Available online: <https://hal.science/hal-01065223/> (accessed on 13 December 2022).
25. Chhipa, A.A.; Chakrabarti, P.; Bolshev, V.; Chakrabarti, T.; Samarin, G.; Vasilyev, A.N.; Ghosh, S.; Kudryavtsev, A. Modeling and Control Strategy of Wind Energy Conversion System with Grid-Connected Doubly-Fed Induction Generator. *Energies* **2022**, *15*, 6694. [[CrossRef](#)]
26. Majout, B.; Bossoufi, B.; Bouderbala, M.; Masud, M.; Al-Amri, J.F.; Taoussi, M.; El Mahfoud, M.; Motahhir, S.; Karim, M. Improvement of PMSG-Based Wind Energy Conversion System Using Developed Sliding Mode Control. *Energies* **2022**, *15*, 1625. [[CrossRef](#)]
27. Gao, Z. Active disturbance rejection control: A paradigm shift in feedback control system design. In Proceedings of the 2006 American Control Conference, Minneapolis, MN, USA, 14–16 June 2006; p. 7. [[CrossRef](#)]
28. Fareh, R.; Al-Shabi, M.; Bettayeb, M.; Ghommam, J. Robust Active Disturbance Rejection Control For Flexible Link Manipulator. *Robotica* **2020**, *38*, 118–135. [[CrossRef](#)]
29. Banks, S.P. A note on non-linear observers. *Int. J. Control.* **1981**, *34*, 185–190. [[CrossRef](#)]
30. Vidyasagar, M. *Nonlinear Systems Analysis/M. Vidyasagar*; Prentice-Hall: Englewood Cliffs, NJ, USA, 1978; p. 302.
31. Machado, D.O.; Chicaiza, W.D.; Escaño, J.M.; Gallego, A.J.; de Andrade, G.A.; Normey-Rico, J.E.; Bordons, C.; Camacho, E.F. Digital twin of a Fresnel solar collector for solar cooling. *Appl. Energy* **2023**, *339*, 120944. [[CrossRef](#)]
32. Chicaiza, W.D.; Dorado, F.; Rodríguez, F.; Gómez, J.; Escaño, J. Detección de ataques de inyección de datos falsos en turbinas eólicas mediante sistemas neuro-borrosos. In *XVII Simposio CEA de Control Inteligente*; Universidad de León: León, Spain, 2022; pp. 66–77. [[CrossRef](#)]
33. Machado, D.O.; Chicaiza, W.D.; Escaño, J.M.; Gallego, A.J.; de Andrade, G.A.; Normey-Rico, J.E.; Bordons, C.; Camacho, E.F. Digital twin of an absorption chiller for solar cooling. *Renew. Energy* **2023**, *208*, 36–51. [[CrossRef](#)]
34. Jang, J.S. ANFIS: Adaptive-network-based fuzzy inference system. *IEEE Trans. Syst. Man Cybern.* **1993**, *23*, 665–685. [[CrossRef](#)]
35. Chiu, S. Fuzzy Model Identification Based on Cluster Estimation. *J. Intell. Fuzzy Syst.* **1994**, *2*, 267–278. [[CrossRef](#)]
36. Loucif, M.; Mechernene, A.; Bossoufi, B. Integral Backstepping Power Control of DFIG Based Nonlinear Modeling Using Voltage Oriented Control. In *Digital Technologies and Applications*; Motahhir, S., Bossoufi, B., Eds.; Springer International Publishing: Cham, Switzerland, 2021; pp. 1725–1734.

Disclaimer/Publisher's Note: The statements, opinions and data contained in all publications are solely those of the individual author(s) and contributor(s) and not of MDPI and/or the editor(s). MDPI and/or the editor(s) disclaim responsibility for any injury to people or property resulting from any ideas, methods, instructions or products referred to in the content.